Integrated Flush Air Data Sensing System Modeling for Planetary Entry Guidance with Direct Force Control

Rafael A. Lugo[*], Christopher D. Karlgaard[†], Richard W. Powell[‡]
Analytical Mechanics Associates, Inc., Hampton, VA 23666

and

Alicia D. Cianciolo[§]
NASA Langley Research Center, Hampton, VA 23681

Flush air data sensing (FADS) systems have been previously used at both Earth and Mars to provide onboard estimates of angle of attack, sideslip angle, and dynamic pressure. However, these FADS data were often not used in an in-the-loop sense to inform the onboard guidance and control systems. A method to integrate FADS-derived density and wind estimates with a numerical predictor-corrector guidance algorithm is presented. The method is demonstrated in a high-fidelity simulation of a human-scale Mars entry vehicle that utilizes a hypersonic inflatable aerodynamic decelerator (HIAD) with direct force control. Effects on guidance commands and state uncertainties both with and without FADS system modeling are presented and discussed.

I.   Introduction

In recent years, there has been an interest in the development of precision landing capabilities with advanced guidance, navigation, and control (GN&C) techniques involving new algorithms and sensors. One type of sensor system that has potential to be utilized for improved flight control is a flush air data sensing (FADS) system. FADS systems have the capability to produce estimates of the freestream atmospheric state conditions by making measurements of the pressure distribution across the forebody, and fitting those measurements to a pressure model. The FADS concept was specifically conceived for use in the hypersonic flight regime where traditional pitot static tubes would be inappropriate for the flow conditions. The development of the concept can be traced to the servo-actuated Q-Ball air data system that successfully flew on the X-15 hypersonic research aircraft [1]. The first successful entry vehicle FADS system was demonstrated during the Shuttle Entry Air Data System (SEADS) project, which flew an instrumented nose cap on five missions on the orbiter OV-102 (Columbia) [2]. Since then, FADS systems have been employed for a wide range of vehicle configurations including high performance aircraft and atmospheric entry vehicles. Recent examples include the Mars Science Laboratory (MSL) [3] and Orion Exploration Flight Test One [4] entry capsules. Past FADS applications have acquired data for use in post-flight trajectory and atmosphere reconstruction. FADS systems have the potential to be utilized in real-time to augment on-board GN&C systems by providing estimates of the wind-relative state and atmosphere [5].

A numerical predictor-corrector (NPC) guidance algorithm has been developed at NASA Langley Research Center (LaRC) as a flexible and robust method of spacecraft aerocapture and entry, descent, and landing (EDL) guidance [6, 7, 8, 9]. The NPC guidance can be used in a direct force control (DFC) sense, meaning that target downrange and crossrange errors can be managed in real-time by modulating angle of attack and angle of sideslip. This approach is particularly effective when the entry vehicle lacks a significant roll moment due to sideslip ($C_{l\beta}$) term, which is generally the case with the entry capsules that have been used for all NASA Mars landing missions to date. The DFC concept is illustrated in Fig. 1.

---

[*] Aerospace Engineer, Atmospheric Flight and Entry Systems Branch, AIAA Member
[†] Supervising Engineer, Atmospheric Flight and Entry Systems Branch, AIAA Senior Member
[‡] Aerospace Engineer, Atmospheric Flight and Entry Systems Branch, AIAA Fellow
[§] Aerospace Engineer, Atmospheric Flight and Entry Systems Branch, AIAA Senior Member

American Institute of Aeronautics and Astronautics
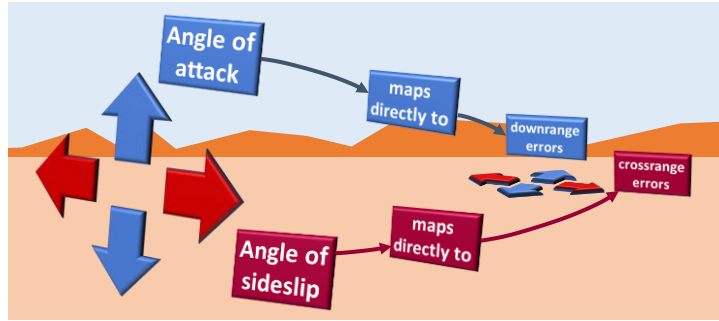
Fig. 1. Direct force control example.

Currently, the NPC guidance uses onboard INS data to estimate the atmospheric properties and aerodynamics, meaning that there are insufficient data to separate the aerodynamics from the atmospheric properties. A method will be presented that integrates FADS-derived atmospheric estimates with the NPC guidance, thus providing the data required to separate aerodynamics from atmospheric properties. Effects on guidance performance and state uncertainties both with and without FADS system modeling are presented and discussed.

II.   Application: Human-Scale Mars Entry

The effects of including an integrated FADS model in an onboard vehicle NPC guidance is evaluated using a human-scale Mars entry vehicle that utilizes a hypersonic inflatable aerodynamic decelerator (HIAD) with DFC achieved by aerodynamic flaps and relevant sensor errors [7-9].

A. Vehicle

The vehicle used in this analysis is a low lift-to-drag ratio (L/D = 0.15) 70° sphere-cone concept that utilizes a HIAD and aerodynamic flaps, shown in Fig. 2. In this figure, the four aerodynamic flaps are shown at the four cardinal locations on the outer edge of the deployed HIAD, shown in beige. The rigid central nosecone is shown in dark gray, with the eight engine nozzles show in a double configuration (the nozzles are shown for illustrative purposes; in flight, they will be sealed until just prior to engine ignition). The habitat payload can be seen to the right, behind the heat shield. When deployed, the HIAD diameter is 16.4 m. Four aerodynamic flaps positioned at 0°, 90°, 180°, and 270° clock angles about the outer edge of the HIAD provide dynamic and trim control and stability. Each flap area is 3% of the vehicle surface area. During powered descent, eight 100 kN engines located in the vehicle centerbody provide supersonic retropropulsion (SRP). For this analysis, aerodynamic effects on the vehicle are not considered during SRP.
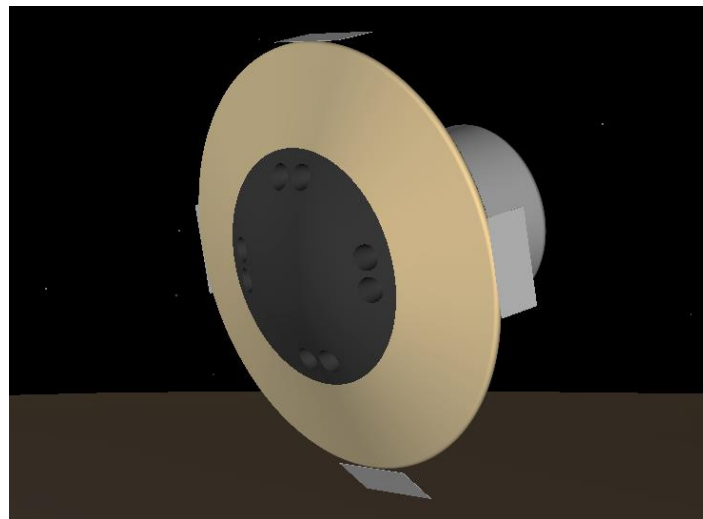
Fig. 2. Representation of the HIAD entry vehicle.

B. Concept of Operations

The crewed entry vehicle performs a deorbit burn at apoapsis of a 1 Sol polar orbit (33793 km apoapsis altitude by 250 km periapsis altitude). After the deorbit burn, the vehicle coasts until atmospheric entry interface (125 km altitude), at which point the simulation atmosphere model (MarsGRAM 2010 [10]) is activated. The guidance and control algorithms are activated when the sensed vehicle acceleration reaches 0.15 g's. Throughout entry, the onboard guidance commands angle of attack and sideslip to control downrange and crossrange targeting errors. At powered descent initiation (PDI), the main engines are activated and the vehicle begins the PD main phase. The PD terminal phase is the final phase, during which the vehicle is directly over the landing site and descends vertically at a constant velocity of 2.5 m/s for 5 s. The EDL concept of operations is shown in Fig. 3.
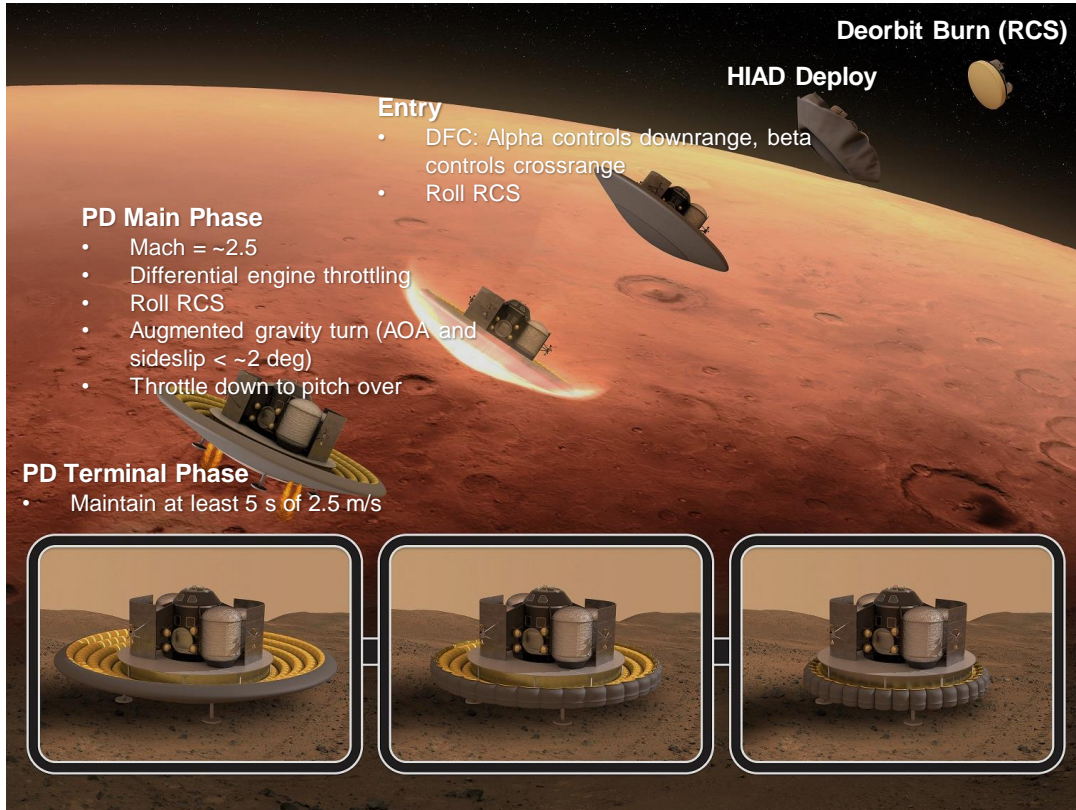

Fig. 3. Human-scale Mars EDL with HIAD vehicle.

Table 1. NPC guidance segments for human-scale Mars EDL with HIAD vehicle.

Segment	Update (Hz)	Start Condition	End Condition	Propagation End	Controls	Targets (at Propagation End)
1	0.2	Sensed G Load	TAEM Acquisition	TAEM Acquisition	Angle of attack Angle of sideslip	Energy at TAEM Zero crossrange
2	0.2	TAEM Acquisition	PDI	Landing	Angle of attack Angle of sideslip Time of PDI	Landing site radius Landing site latitude Landing site longitude
3	1.0	PDI	Throttle Down	Landing	Angle of attack Angle of sideslip Net engine thrust	Landing site radius Landing site latitude Landing site longitude
4	1.0	Throttle Down	Terminal Phase	Landing	Velocity at throttle down Throttle setting at throttle down	Pitch angle at terminal descent Landing site radius
5	1.0	Terminal Phase	Landing	Landing	--	--

The entry trajectory was divided into segments for the onboard NPC guidance, listed in Table 1. The guidance was designed so that the command update frequency can be changed at segments, so that commands during unpowered

American Institute of Aeronautics and Astronautics

flight are issued at larger intervals than during powered flight (where the vehicle dynamics occur much faster). Additionally, the trajectory propagation endpoints can differ from the guidance segment end conditions. Specifically, for most of the simulation, the guidance is internally propagating the vehicle trajectory to landing, rather than just to the next waypoint. Thus, the guidance is continually targeting parameter conditions at the end of the propagated trajectory (usually landing), rather than simply the next waypoint. Note that for this study, the flight phase of terminal area energy management (TAEM) is the period during which the vehicle has already performed the pull-out maneuver that targets the peak G load and is now determining when to start the engines so that the spacecraft will land at the desired location.

From Table 1 it is clear that different controls were used to achieve different targets depending on the segment. For example, Segment 2, which starts at TAEM acquisition, is modulating angle of attack and sideslip as well as the time of PDI to minimize the landing site targeting errors (this is an example of DFC). After PDI, the guidance transitions to Segment 3 and the time of PDI control is changed to the net engine thrust, but the targets remain the same. A throttle-down phase was used to permit targeting of a vertical pitch angle at the start of the terminal phase. During this final phase (Segment 5), the vehicle holds a constant velocity of 2.5 m/s and side velocities are nulled to descend vertically, and no further commands are issued.

III.   System Modeling

To date, the trajectory design assumptions in Refs. [7-9] have included perfect navigation data, meaning that the guidance has perfect knowledge of the vehicle state at every guidance update. In this paper, an effort is made to introduce relevant sensor errors and to quantify their effects on overall vehicle performance. To that end, the NPC guidance, the methods of modeling the air data sensors, and the FADS system estimation algorithm are detailed here.

A. Guidance

The guidance used in the simulation is an NPC guidance currently in development at NASA Langley Research Center. This guidance uses waypoint targets obtained from a reference three-degree-of-freedom (3DOF) trajectory that optimizes performance (e.g., maximum mass to surface) and satisfies trajectory constraints such as G-load limits. The waypoint targets are then loaded into the guidance, which utilizes an internal projected gradient algorithm to solve for the combination of guidance commands that satisfy the targets. Trajectories required for NPC targeting are propagated internally using simplified 3DOF equations of motion.

Waypoint definitions are selected by the analyst and are highly dependent on the type of trajectory (e.g., aerocapture, entry, powered descent) and type of vehicle (e.g., blunt body, slender body). The periods of the trajectory between waypoints are referred to in this work as segments. Each guidance segment can have different guidance controls and constraints. See Table 1 for a description of the various guidance segments used in the trajectory simulation.

A flowchart illustrating the logic flow of the NPC guidance is shown in Fig. 4. Note that in this study, the FADS-derived atmosphere estimates will overwrite the density estimates obtained from the vehicle accelerations.
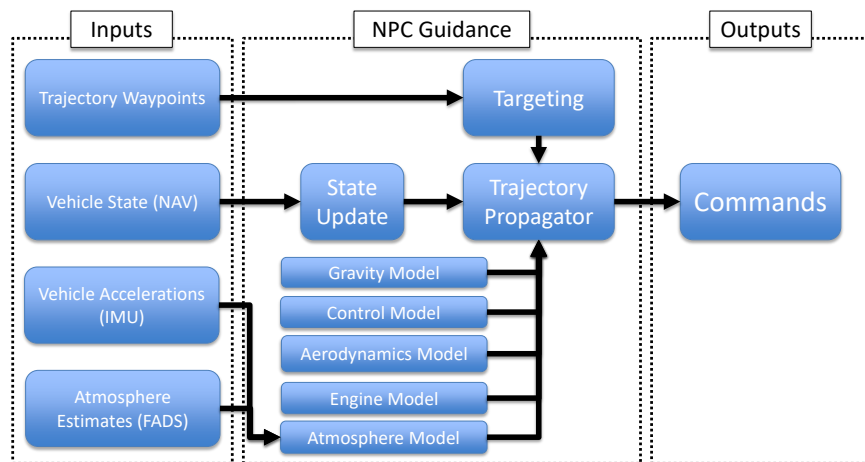
Fig. 4. Outline of NPC guidance logic.

The NPC guidance obtains an estimate of the atmospheric density by using the IMU-derived sensed axial acceleration and onboard aerodatabase to solve the following equation

$$\rho_\infty = \frac{2ma_x}{V_\infty^2 C_A S} \tag{1}$$

where m is the vehicle mass, a_x is the sensed axial acceleration obtained from the onboard accelerometers and smoothed using a 40 s running mean, V_∞ is the vehicle velocity relative to the planet obtained from the onboard navigation estimate, C_A is the axial force coefficient obtained from the onboard aerodatabase, and S is the vehicle aerodynamic reference area. This computed density is then used to modify the onboard reference density model. This updated reference density is then used in the propagated trajectories internal to the NPC guidance. Thus, the NPC guidance can correct for deviations in the actual atmosphere using accelerometer data. In the present analysis, the computed density from accelerometers is replaced with the density obtained from the FADS system, and a comparison is made between the two approaches.

B. Flush Air Data Sensing System

The FADS pressure port layout used for this study consists of a cruciform array of nine ports located on the vehicle forebody shown in Fig. 5. These ports are arrayed with one located at the geometric center of the heatshield and the other eight ports in two sets of symmetric rings in the pitch and yaw planes. The inner ports are intended to capture the expected range of the stagnation point as the NPC guidance issues angle of attack and sideslip commands. The outer ports are intended to provide observability of the flow angles and are placed as far outboard as possible without interfering with hardware constraints.
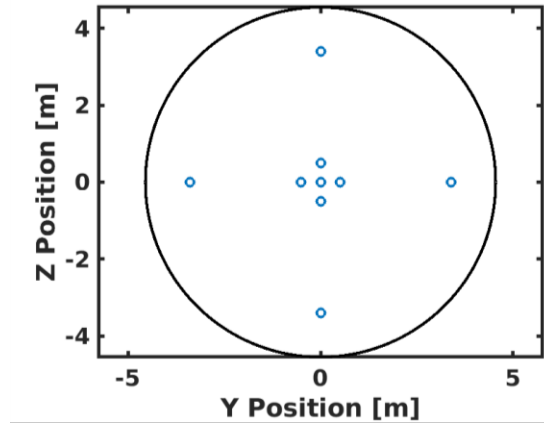

Fig. 5. FADS Pressure Port Layout.

The pressure distribution across the forebody can be approximated using modified Newtonian flow theory. The pressure at port *i* is given by the equation [11]

$$p_i = p_t[(1 - R)\cos^2\theta_i + R] \tag{2}$$

where p_t is the total pressure, $R = p_s/p_t$ is the ratio of static (or freestream) to total pressure, and θ_i is the incidence angle of the flow at the given port location. The incidence angle is a function of the flow angles, given by

$$\cos\theta_i = \cos\alpha\cos\beta\cos\lambda_i + \sin\beta\sin\phi_i\sin\lambda_i + \sin\alpha\cos\beta\cos\phi_i\sin\lambda_i \tag{3}$$

where λ_i is the port cone angle, ϕ_i is the port clock angle, α is the angle of attack, and β is the angle of sideslip. The pressure ratio R is a function of the freestream Mach number, given by the equation

$$R = \begin{cases} \left[\dfrac{2}{(\gamma+1)M^2}\right]^{\gamma/(\gamma-1)} \left[\dfrac{2\gamma M^2 - (\gamma-1)}{\gamma+1}\right]^{1/(\gamma-1)} & \text{for } M > 1 \\[2em] \left[1 + \left(\dfrac{\gamma-1}{2}\right)M^2\right]^{-\gamma/(\gamma-1)} & \text{for } M \leq 1 \end{cases} \qquad (4)$$

where M is the freestream Mach number and γ is the ratio of specific heats (for Mars this is approximated as a constant 1.333).

The port pressures evaluated along the nominal trajectory are shown as a function of time in Fig. 6. Note that these pressure ranges are similar to those for which the MEDLI2 supersonic pressure transducers are designed to operate [12].
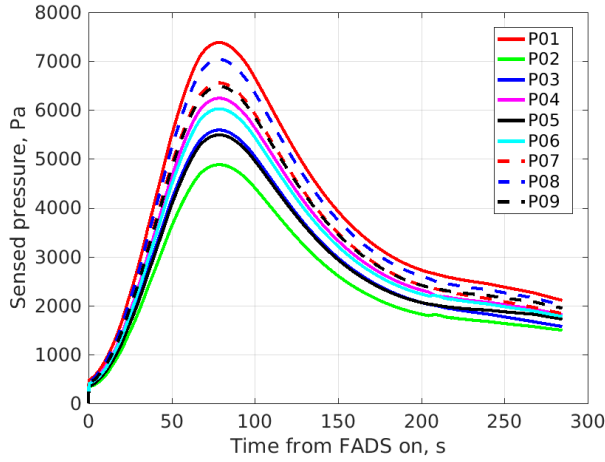
Fig. 6. Nominal sensed port pressures.

The air data are assumed to be measured by pressure transducers similar in performance to those flown on the MEDLI system in the MSL heatshield [13] but configured for full scale ranges appropriate to this entry vehicle. The error model used for this study assumes a 3σ scale factor uncertainty of 0.5% of reading and 3σ random measurement noise of 5 Pa. Note that the MEDLI2 system that will be flown on Mars 2020 3σ scale factor uncertainty is expected to be 0.25%. Pneumatic lags are not modeled in this study. System latencies are captured by implementation of the FADS system processing algorithm in the flight software, as described in the next subsection.

C. Air Data State Estimation Algorithm
The nine measured FADS pressures yield an overdetermined system of nonlinear algebraic equations that can be solved using a nonlinear least squares technique to produce an estimate of the freestream atmospheric-relative state [3]. The freestream state can be defined as

$$\boldsymbol{x} = \{q_\infty \quad p_\infty \quad \alpha \quad \beta\}^T \qquad (5)$$

where q_∞ is dynamic pressure and p_∞ is the freestream pressure. The modified Newtonian flow equations can be expressed as

$$\boldsymbol{p} = \boldsymbol{h}(\boldsymbol{x}) \qquad (6)$$

where $\boldsymbol{p} = \{p_1 \quad \cdots \quad p_N\}^T$. The pressure model can be linearized about a reference state $\overline{\boldsymbol{x}}$ to yield

$$\boldsymbol{p} = \boldsymbol{h}(\overline{\boldsymbol{x}}) + H(\boldsymbol{x} - \overline{\boldsymbol{x}}) \qquad (7)$$

where $H = \partial \boldsymbol{h}/\partial \boldsymbol{x}$. The terms can be rearranged to yield a linear regression problem of the form

$$\boldsymbol{y} = H\boldsymbol{x} \qquad (8)$$

where $\boldsymbol{y} = \boldsymbol{p} - h(\overline{\boldsymbol{x}}) + H\overline{\boldsymbol{x}}$. The problem can then be solved using the least squares estimator, given by

$$\hat{\pmb{x}} = (H^T W H)^{-1} H^T W \pmb{y} \qquad (9)$$

where W is the measurement weighting matrix (usually the inverse of the measurement covariance matrix). The solution can be iterated at each measurement by replacing $\bar{\pmb{x}}$ with $\hat{\pmb{x}}$ until the estimate converges or a predetermined iteration threshold has been reached (convergence is not guaranteed). The guidance states can then be updated with the air data state estimates. In particular, the freestream density ρ_∞ can be approximated (assuming zero winds) from the converged dynamic pressure by the equation

$$\rho_\infty = \frac{2q_\infty}{V_\infty^2} \qquad (10)$$

where V_∞ is the magnitude of the velocity computed from the on-board navigation. Note that an advantage of the FADS system method is that the estimated angle of attack and sideslip are wind-relative, rather than planet-relative quantities derived from the accelerometers, though the effects of this are likely to be small in the hypersonic regime.

IV. Trajectory Simulation

High-fidelity, six-degree-of-freedom (6DOF) trajectories were simulated in the Program to Optimize Simulated Trajectories II (POST2), an event-driven, point-mass trajectory simulation software with discrete parameter targeting and optimization capability [14]. The POST2 simulation was executed at an integration rate of 100 Hz. The various models were queried at specific frequencies, listed in Table 2, to simulate actual flight software (differing frequencies are possible but not investigated in the present study). At every simulation time step, the models for the FADS sensors, navigation filter, FADS estimator, and guidance were queried, in that order.

Table 2. Simulation model call rates.

System	Frequency (Hz)
Simulation	100
FADS Pressure Sensors	100
Navigation Filter	100
FADS Estimator	100
Guidance	0.2

A. FADS Pressure Sensors

The nine FADS pressure sensors were modeled using the modified Newtonian flow approximations described in Section II.A. The resultant data were corrupted to simulate actual an actual FADS pressure sensor by applying white noise and scale factors to each sensor output. Biases were not applied because they will be removed prior to entry with an in-flight zero. The FADS pressure sensors were activated when the dynamic pressure estimate reached 250 Pa (approximately Mach 24.5), and deactivated at PDI (approximately Mach 2.5).

B. Navigation Filter

A "perfect" navigation filter was implemented that duplicated the simulation calculations for the various vehicle states and parameters required by the vehicle guidance, controllers, and other flight software. Perfect vehicle states (position, velocity, and attitude) were queried from the simulation at the navigation filter frequency. Derived states and parameters such as angle of attack, range to target, and "sensed" body accelerations, were computed using the same or similar equations as in POST2. In the specific case of the body accelerations, "measurement" errors in the form of noise, biases, and scale factors were applied. All other quantities were left uncorrupted. Note that the body accelerations were not used in the navigation filter to obtain a state estimate and were used only in the guidance algorithm to correct density as described in Section II.C.

A simulation flag informed the navigation filter to use FADS-derived dynamic pressure, freestream pressure, freestream density, angle of attack, angle of sideslip, and Mach number if the FADS estimator was active during that simulation time step. Otherwise, the perfect-state derived quantities for these parameters were used.

C. FADS Estimator

The FADS estimator was modeled using the least squares approach described in Section II.B. The iterative algorithm was limited to 10 iterations, and was considered converged when the root-sum-squared value of the estimate changes was equal to or less than 0.1. The FADS estimator was active during the period when the FADS pressure sensors were active (dynamic pressure greater than 250 Pa and prior to PDI). At every FADS estimator call, the

estimator updated the navigation filter values for dynamic pressure, freestream pressure, freestream density, angle of attack, angle of sideslip, and Mach number. For this study, the measurement covariance was an identity matrix, meaning that the weights were assumed to be uncorrelated and time-invariant.

D. Guidance

The vehicle guidance was modeled using the numerical predictor-corrector approach described in Section II.C. A simulation flag informed the guidance when the FADS estimator was active use the FADS-derived density to obtain the density correction, rather than to estimate the correction from the sensed axial acceleration.

E. Monte Carlo Analysis

Monte Carlo analyses were performed by applying dispersions to parameters in the nominal trajectory. The dispersions used to generate the Monte Carlo trajectories are listed in Table 3. The initial states at deorbit consisted of inclination, longitude of the ascending node, periapsis and apoapsis altitude, true anomaly, and argument of periapsis.

Table 3. Monte Carlo dispersions.

Category	Parameter	Dispersion	Distribution
Initial Conditions	Deorbit burn execution	0.135 m/s 3σ	normal
	Uncorrelated state covariance	0.03° 3σ for angles, 0.03 km 3σ for altitudes	normal
Atmosphere	Density	MarsGRAM	--
	Winds	MarsGRAM	--
	Dusttau	0.1:0.9	uniform
Aerodynamics	Aerodatabase uses coefficient multipliers and adders for different aerodynamic regimes based on CFD, wind tunnel tests, and flight data from similar shapes	--	--
Propulsion	Peak thrust	Scale factor: 1% 3σ	normal
	Peak Isp	Scale factor: 1% 3σ	normal
	Start lag time	0.0:0.2 s	uniform
	Startup transient rate	Scale factor: 1% 3σ	normal
	Main phase response rate	Scale factor: 1% 3σ	normal
Sensors	Sensed accelerations [8]	Noise: 0.6 m/s^2 3σ Bias: 300 µg 3σ Scale factor: 525 ppm 3σ	normal normal normal
	FADS	Noise: 5 Pa 3σ Scale factor: 0.5% 3σ	normal normal
Mass	Mass	500 kg 3σ	normal
	Center of gravity	0.05 m 3σ	normal
	Moments of inertia	5% kg-m^2 3σ	normal

V.   Results

Three cases were examined for this analysis in a Monte Carlo sense:

1. A case with the guidance using perfect accelerometer data to estimate density (noted as BSLN in figures)
2. A case with the guidance using corrupted accelerometers data (scale factors, biases, and noise) to estimate density (noted as ACC in figures)
3. A case with the guidance using corrupted FADS-derived density (scale factors and noise) (noted as FADS in figures)

For each of these cases, an 8,001-trajectory Monte Carlo (one nominal and 8,000 dispersed runs) was run using the dispersion listed in Table 3. Relevant statistics are various events along the trajectory were computed and are shown and discussed in this section.

Figure 7 shows the comparison between the FADS-derived estimates for angle of attack, angle of sideslip, dynamic pressure, and freestream pressure in black and the truth values in red for an arbitrary trajectory out of the

8,001 runs. The results indicate that even with corrupted pressure measurements, the FADS estimation algorithm provides solutions that agree with the truth data. The noise in the solution is apparent in total pressure (noise is not present in the truth freestream pressure because MarsGRAM does not perturb pressure, but perturbs density).
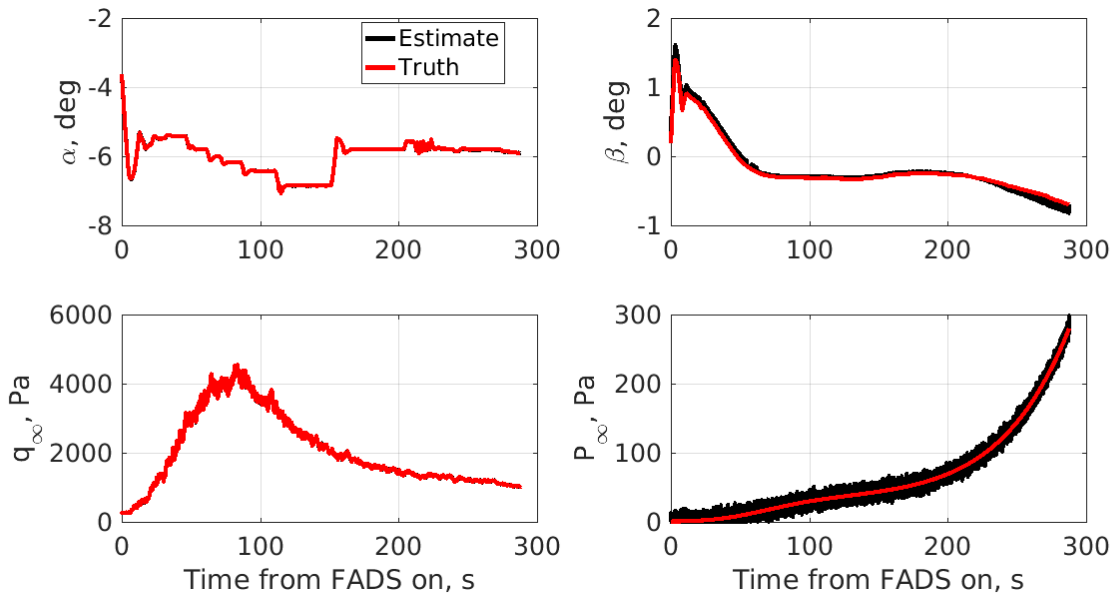
Fig. 7. Comparison of FADS-derived estimates to truth values, dispersed trajectory.

Figure 8 shows a comparison of the errors between the estimated and true densities from the three Monte Carlo analyses for a selected dispersed case. Note that the baseline case, with perfect accelerometers, does not show zero errors because the guidance is applying a 40 s running mean to the sensed accelerations. It is evident that the corrupted accelerometer case tracks the perfect accelerometer case, but with more noise. The accelerometer-derived density errors are both larger in magnitude and noisier than those from the FADS-derived approach, indicating that the FADS system approach provides a more accurate density estimate given the sensor uncertainties listed in Table 3.
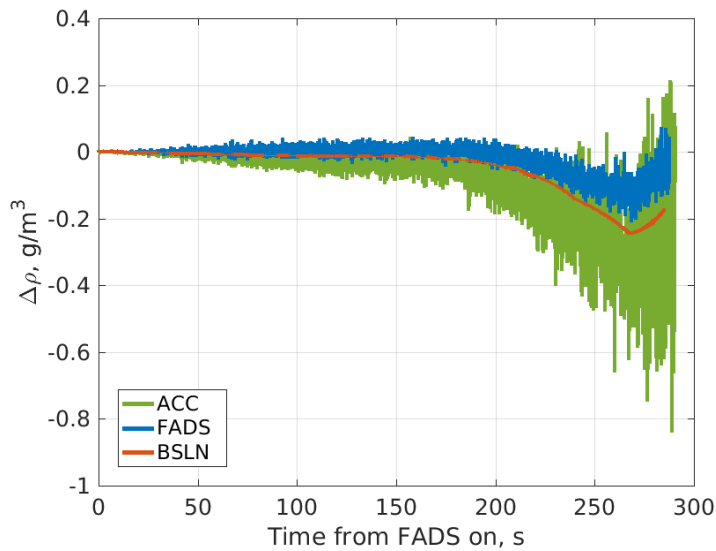

Fig. 8. Errors between estimated and true density, accelerometer-derived and FADS-derived.

It is useful to compare how the FADS estimator can improve the overall vehicle behavior. A dispersed case was chosen specifically to illustrate an improvement and is shown in Fig. 9. The corrupted accelerometer angle of attack

9

American Institute of Aeronautics and Astronautics

profile, shown in green, follows the baseline profile, shown in red, until approximately 120 seconds after the FADS system is activated (time zero). At this point, the corrupted accelerometer case diverges and displays more dynamic angle behavior until approximately 210 s, after which the angle of attack begins to oscillate between -9 and -8 degrees, indicating that the guidance solutions for angle of attack commands are reaching the command bounds. Recall that the accelerometer cases are not integrating the accelerations to obtain vehicle states as in traditional spacecraft navigation filters, and are only using the accelerations to update the guidance density estimate. The angle oscillations and the guidance commands hitting their limits are undesirable vehicle behavior.

The same dispersed case, but using corrupted FADS data, is shown in blue. While it does not follow the baseline case perfectly, as soon as the angles of attack diverge the vehicle is flying a different trajectory. This case exhibits angle of attack behavior that is much less dynamic, and illustrates how using the FADS-derived solutions can improve overall vehicle behavior.
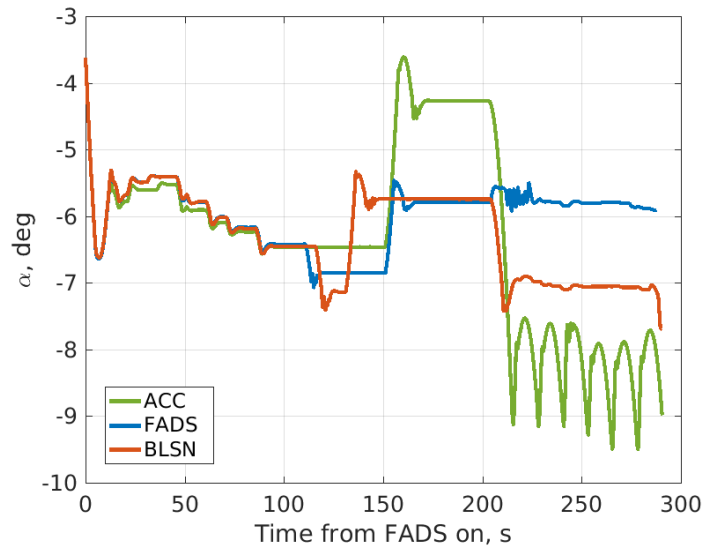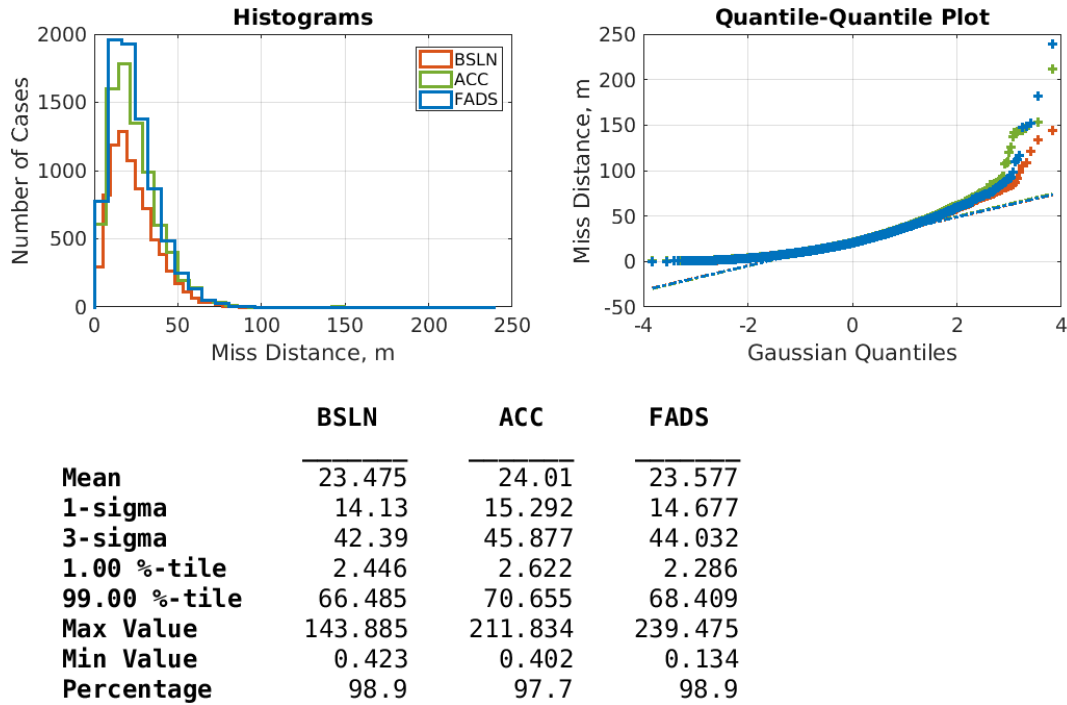

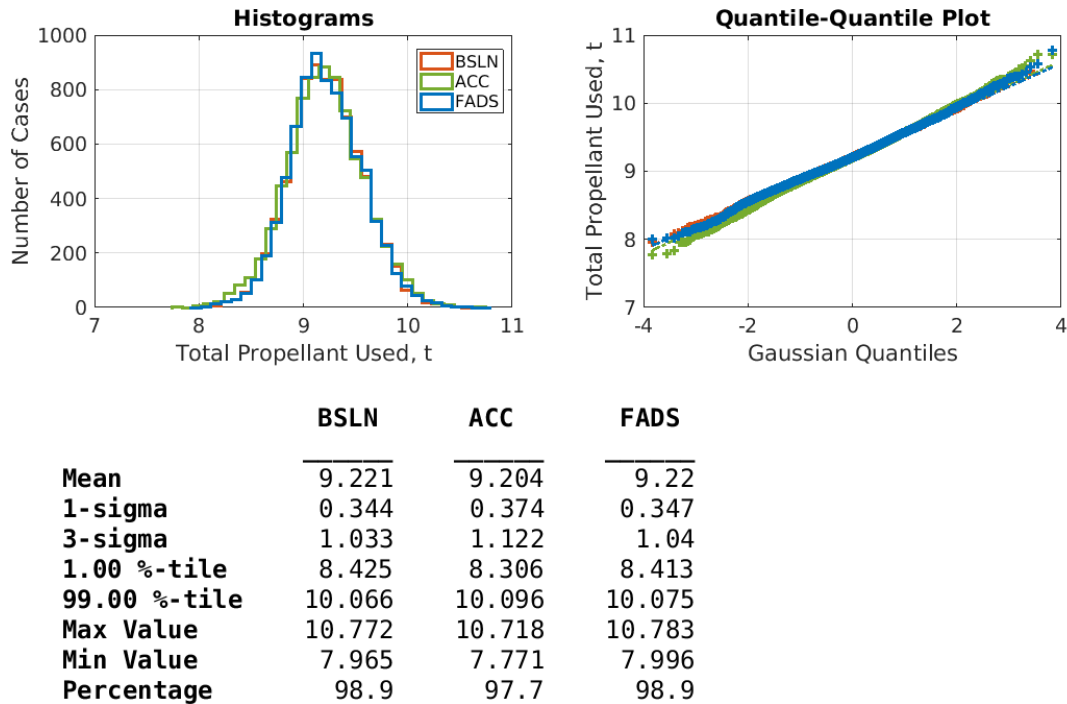**Fig. 9. Comparison of angle attack profiles, dispersed case.**

The results of the Monte Carlo simulations are shown in the following figures. In these figures, the top left plot is the histogram, the top right plot is a quantile-quantile plot that provides an indication of how close the distribution is to Gaussian (perfectly Gaussian is shown by the dashed line that is the same color as the histogram), and relevant statistics are shown below the plots.

A comparison of the landing site miss distance between the three Monte Carlo cases is shown in Fig. 10, and there are several elements to note. The "percentage" value is the percentage of the 8,001 trajectories that were considered "successful," which in this case means any case that landed with a non-zero final mass. Thus, of the 8,001 trajectories run for each Monte Carlo, 1.1% of them failed in the baseline case (perfect accelerations), and 2.3% failed when acceleration errors were added. When FADS-derived solutions were introduced to replace those derived from the accelerations, the failed cases were reduced back to match the baseline, 1.1%.

Since the distribution here is non-Gaussian, it is useful to inspect the percentiles rather than the standard deviations. The 99%-tile highs show that there is a small but noticeable reduction in landing accuracy when adding accelerometer errors, raising the miss distance from 66.5 m to 70.7 m. However, when FADS estimates are introduced, this miss distance is reduced to 68.4 m. While the accuracy from the perfect accelerometer case is not regained with a FADS system, it is an improvement over the corrupted accelerometer case. It is also notable that there are fewer outliers on the higher end in the FADS case, shown in the quantile-quantile plot, though there is a single outlier with a larger miss distance than the other two cases. Thus, in terms of landing accuracy, the FADS approach provides an improvement.

	BSLN	ACC	FADS
Mean	23.475	24.01	23.577
1-sigma	14.13	15.292	14.677
3-sigma	42.39	45.877	44.032
1.00 %-tile	2.446	2.622	2.286
99.00 %-tile	66.485	70.655	68.409
Max Value	143.885	211.834	239.475
Min Value	0.423	0.402	0.134
Percentage	98.9	97.7	98.9

Fig. 10. Comparison of landing site miss distance.

	BSLN	ACC	FADS
Mean	9.221	9.204	9.22
1-sigma	0.344	0.374	0.347
3-sigma	1.033	1.122	1.04
1.00 %-tile	8.425	8.306	8.413
99.00 %-tile	10.066	10.096	10.075
Max Value	10.772	10.718	10.783
Min Value	7.965	7.771	7.996
Percentage	98.9	97.7	98.9

Fig. 11. Comparison of total propellant used.

A comparison of the total propellant used is shown in Fig. 11. Of note in this figure is the apparent mean propellant usage improvement between the baseline and corrupted accelerometer cases, which is perhaps counter-intuitive as additional errors should in general lead to worse performance. This improvement is potentially misleading, however, when two additional statistics are considered. One, recall that the corrupted accelerometer case has more failed cases than the other two cases, meaning that while there is a small overall propellant usage improvement, fewer cases

American Institute of Aeronautics and Astronautics

actually landed with a non-zero mass. Two, note the standard deviation, which is relevant here since the distributions are close to Gaussian. With accelerometer errors, the uncertainty grows from 0.34 to 0.37 t. When using FADS estimates, the error reduces back to 0.35 t, essentially recovering the performance with perfect accelerometers. Additionally, the 99%-tile is improved when using a FADS system over corrupted accelerometers. However, note that the differences here are small (on the order of tens of kilograms), so the benefits of a FADS system over accelerometers are modest in terms of propellant usage.

The next Monte Carlo comparisons relate back to landing site miss distance in Fig. 10. First, a parameter that illustrates the effect of density estimation accuracy on guidance performance is the commanded main engine throttle setting at PDI, shown in Fig. 12. Recall from Table 1 that during the TAEM phase, the guidance is attempting to target the landing site by adjusting the time of main engine start. Prior to when the engines are actually commanded on, the guidance assumes that the throttle setting is a constant 80% and that the vehicle flies a pure gravity turn during the PD main phase. The instant the engines are commanded on and the PD main phase guidance segment is entered, the guidance begins to modulate the main engine throttle setting to target the same landing site (note that angle of attack and sideslip are also modulated in both of these segments to improve targeting accuracy). Thus, any deviation in the new main engine throttle setting from 80% is an indicator that the guidance has not correctly accounted for vehicle or environment dispersions. A significant driver of error is the density estimate.

In Fig. 12, the comparison of this initial commanded throttle setting at PDI is shown. Here, the effects of the FADS approach on outliers is evident. Adding corrupted accelerometer data increases the outliers on both ends of the distribution, while introducing FADS-derived density estimates significantly reduces them. While the effects on the high and low percentiles is not significant, the result is that using a FADS system can improve the ability of the guidance to estimate the atmosphere and therefore better target PDI.

	BSLN	ACC	FADS
Mean	78	78	78
1-sigma	0	1	0
3-sigma	1	2	1
1.00 %-tile	78	77	78
99.00 %-tile	79	79	79
Max Value	80	82	80
Min Value	73	59	68
Percentage	98.9	97.7	98.9
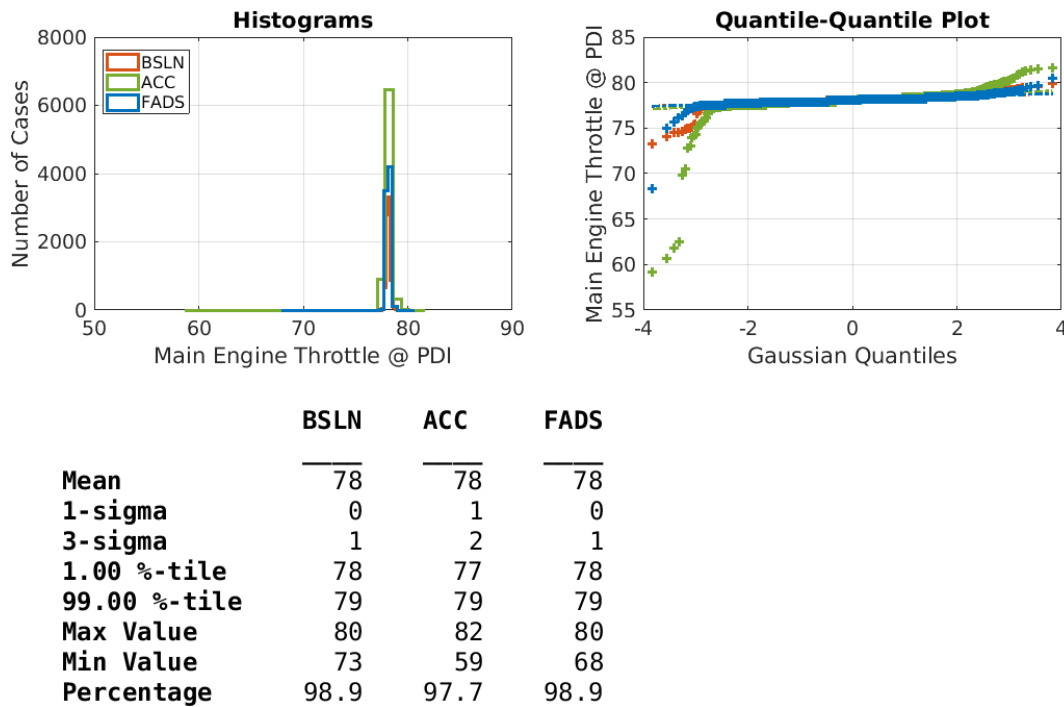
Fig. 12. Comparison of main engine throttle setting at PDI.

In Fig. 13 and Fig. 14 the comparison between vehicle altitude at PDI and vehicle planet-relative velocity, respectively, are shown. While the tails prevent the distributions from being strictly Gaussian, the standard deviations show that using a FADS system provides a significant improvement in the altitude (essentially regaining the performance from the perfect accelerometer case) and a modest improvement in velocity uncertainty over using corrupted accelerometers. This is also supported by the change in the differences between the high and low percentiles. To understand the implication of this, recall that the reference trajectory uses a pure gravity turn from PDI to the start of the PD terminal phase, and that any dispersions will cause the guidance to modify the pure gravity turn with small planet-relative angles of attack and sideslip to attempt to improve landing site targeting accuracy. Thus, smaller

altitude-velocity dispersions at PDI result in better landing accuracy because the guidance will command the vehicle to fly closer to the reference trajectory.
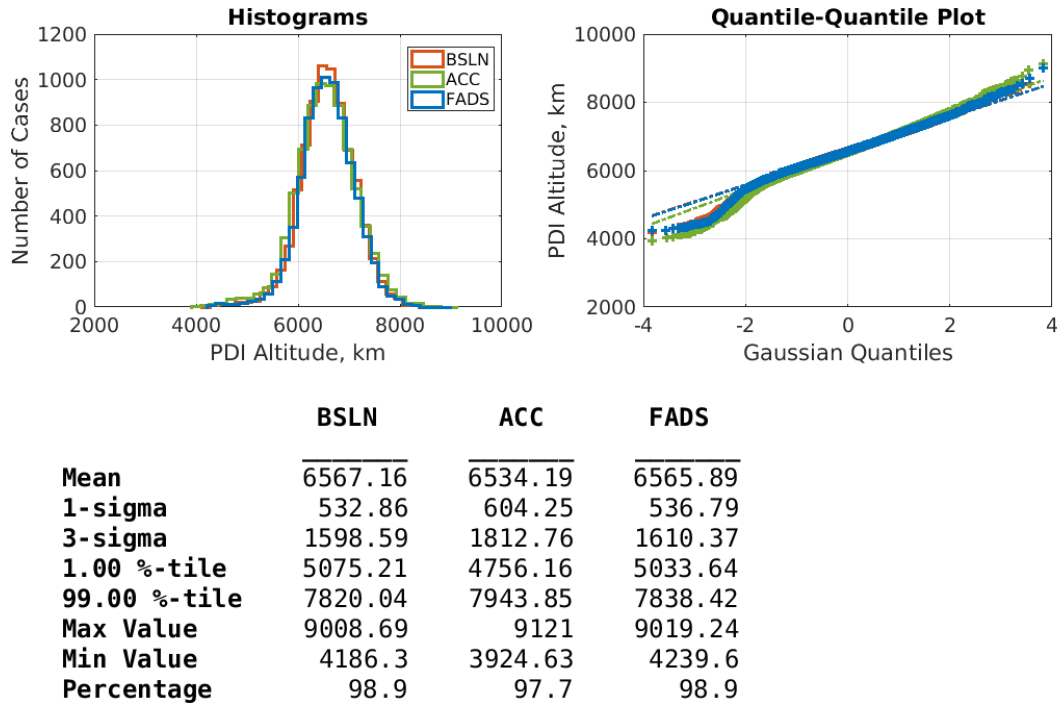

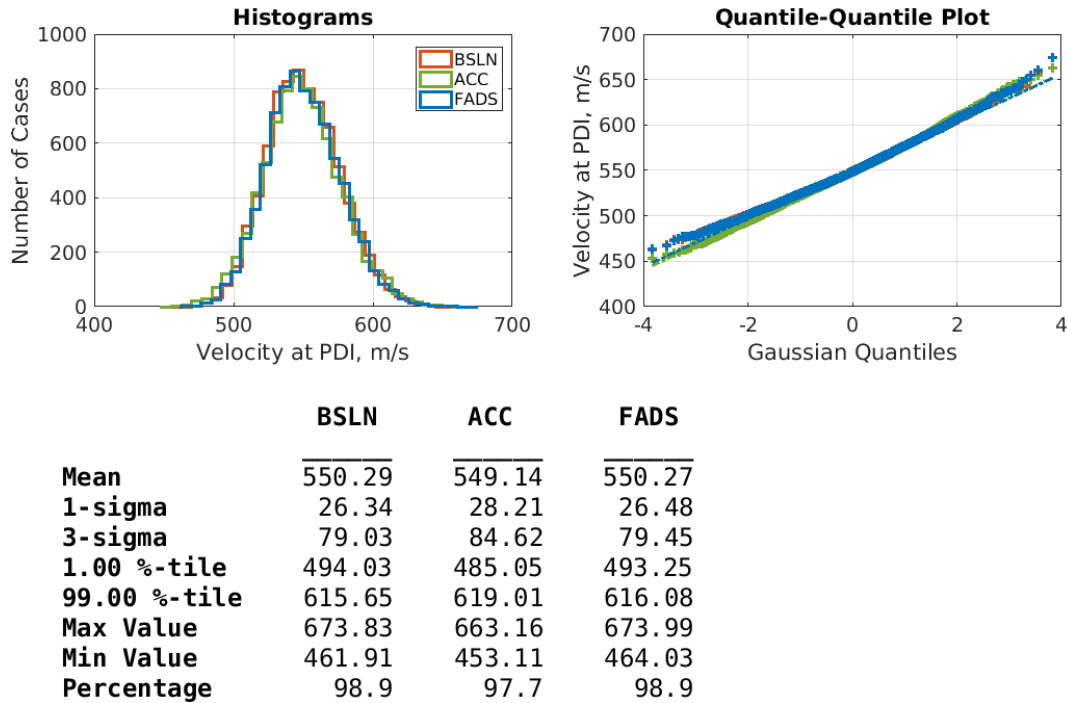|	BSLN	ACC	FADS
Mean	6567.16	6534.19	6565.89
1-sigma	532.86	604.25	536.79
3-sigma	1598.59	1812.76	1610.37
1.00 %-tile	5075.21	4756.16	5033.64
99.00 %-tile	7820.04	7943.85	7838.42
Max Value	9008.69	9121	9019.24
Min Value	4186.3	3924.63	4239.6
Percentage	98.9	97.7	98.9

Fig. 13. Comparison of altitude at PDI.

	BSLN	ACC	FADS
Mean	550.29	549.14	550.27
1-sigma	26.34	28.21	26.48
3-sigma	79.03	84.62	79.45
1.00 %-tile	494.03	485.05	493.25
99.00 %-tile	615.65	619.01	616.08
Max Value	673.83	663.16	673.99
Min Value	461.91	453.11	464.03
Percentage	98.9	97.7	98.9

Fig. 14. Comparison of planet-relative velocity at PDI.

American Institute of Aeronautics and Astronautics

VI.   Summary and Conclusions

This paper has demonstrated that an overall improvement in guidance performance and a reduction in trajectory uncertainties over using corrupted accelerometers can be achieved by introducing a FADS system model into the onboard GN&C platform. Specifically, using a FADS system enabled the guidance to more accurately internally model and propagate the vehicle trajectory, which mitigated large angle of attack oscillations and tighter targeting of PDI. This also improved altitude and velocity uncertainties at PDI and landing site miss distance. Modest propellant usage improvements were also noted. In all of these cases, the use of FADS-derived estimates essentially restored the vehicle performance to that when using perfect accelerometer data.

It is expected that better approximations of a realistic entry system can be modeled within the current simulation framework. Specifically, the modified Newtonian flow approximation can be replaced with CFD-derived pressure model tables. The least squares algorithm can be replaced with a Kalman filter implementation that blends multiple types of data together to provide the guidance and controllers with a "best estimate" and associated uncertainties [3]. The FADS sensor model fidelity can be improved by implemented hysteresis and pneumatic lag present in actual pressure transducers. The relatively simple sensed acceleration model (embedded in the navigation filter) can be replaced with a discrete IMU model with misalignments.

References

[1]   Cary, J. P. and Keener, E. R., "Flight Evaluation of the X-15 Ball-Nose Flow-Direction Sensor as an Air-Data System," NASA TN-D-2923, July 1965.

[2]   Siemers, P., Henery, M. W., and Eades, J. B., "Shuttle Entry Air Data System (SEADS) – Advanced Air Data System Results: Air Data Across the Entry Speed Range," *Orbiter Experiments (OEX) Aerothermodynamics Symposium,* NASA CP-3248, Part I, April 1995, pp. 49-78.

[3]   Karlgaard, C. D., Kutty, P., Schoenenberger, M., Munk, M. M., Little, A., Kuhl, C., and Shidner, J., "Mars Science Laboratory Entry Atmospheric Data System Trajectory and Atmosphere Reconstruction," *Journal of Spacecraft and Rockets*, Vol. 51, No. 4, 2014, pp. 1029-1047.

[4]   Bibb, K., Cassady, L. D., and Schwing, A. M., "Orion EFT-1 FADS-Based Trajectory Reconstruction," AIAA Paper 2016-3989, June 2016.

[5]   Karlgaard, C. D., Kutty, P., and Schoenenberger, M., "Coupled Inertial Navigation and Flush Air Data Sensing Algorithm for Atmosphere Estimation," *Journal of Spacecraft and Rockets*, Vol. 54, No. 1, 2017, pp. 128-140.

[6]   Fraysse, H., Powell, R., Rosseau, S., and Striepe, S., "CNES-NASA Studies of the Mars Sample Return Orbiter Aerocapture Phase," 51st International Astronautical Congress, 2-6 October, 2000, Rio De Janeiro, Brazil, IAF-00-A.6.05.

[7]   Cianciolo, A. D., and Polsgrove, T. T., "Human Mars Entry, Descent, and Landing Architecture Study Overview," AIAA SPACE 2016, 13-16 September 2016, Long Beach, CA, 10.2514/6.2016-5494.

[8]   Cianciolo, A., Striepe, S., Carson, J., Sostaric R., Woffinden, D., Karlgaard, C., Lugo, R., Powell, R., and Tynis, J., "Defining Navigation Requirements for Future Precision Lander Missions," SciTech 2019 AIAA Paper, submitted for publication, January 2019.

[9]   Cianciolo, A. D., and Powell, R. W., "Entry, Descent, and Landing Guidance and Control Approaches to Satisfy Marsk Human Mission Landing Criteria," AAS-17-254.

[10] Justus, C. G., "Mars Global Reference Atmospheric Model for Mission Planning and Analysis," J. Spacecraft, Vol. 28, No. 2, pp. 216-21, March-April 1991.

[11] Pruett, C. D., Wolf, H., Heck, M. L., and Siemers, P. M., "Innovative Air Data System for the Space Shuttle Orbiter," *Journal of Spacecraft and Rockets*, Vol. 20, No. 1, 1983, pp. 61-69.

[12] Hwang, H., H., Bose, D., White, T. R., Wright, H., Schoenenberger, M., Kuhl, C. A., Trombetta, D., Santos, J. A., Oishi, T., Karlgaard, C. D., Mahzari, M., and Pennington, S., "Mars 2020 Entry, Descent, and Landing Instrumentation 2 (MEDLI2)," AIAA Paper 2016-3536, June 2016.

[13] Karlgaard, C. D., Van Norman, J., Siemers, P., M., and Schoenenberger, M., "Mars Entry Atmospheric Data System Modeling, Calibration, and Error Analysis," NASA TM-2014-218537, October 2014.

[14] Lugo, R. A., Shidner, J. D., Powell, R. P., Marsh, S. M., Hoffman, J. A., Litton, D. K., and Schmitt, T. L., "Launch Vehicle Ascent Trajectory Simulation Using The Program to Optimize Simulated Trajectories II (POST2)," AAS 17-274.